

# Statistics of simulated and observed pair separations in the Gulf of Mexico

FRANCISCO J. BERON-VERA\*

*Department of Atmospheric Sciences, Rosenstiel School of Marine and Atmospheric Science, University of Miami, Miami, Florida, USA.*

J. H. LACASCE

*Department of Geosciences, University of Oslo, Oslo, Norway.*

## ABSTRACT

Pair-separation statistics of in-situ and synthetic surface drifters deployed near the *Deepwater Horizon* site in the Gulf of Mexico are investigated. The synthetic trajectories derive from a 1-km-resolution data-assimilative Navy Coastal Ocean Model (NCOM) simulation. The in-situ drifters were launched in the Grand Lagrangian Deployment (GLAD). Diverse measures of the dispersion are calculated and compared to theoretical predictions. For the NCOM pairs, the measures indicate nonlocal pair dispersion (in which pair separations grow exponentially in time) at the smallest sampled scales. At separations exceeding 100 km, pair motion is uncorrelated, indicating absolute rather than relative dispersion. With the GLAD drifters however the statistics are ambiguous, with some indicating local dispersion (in which pair separations exhibit power law growth) and others suggesting nonlocal dispersion. The difference between the two data sets stems in part from inertial oscillations, which affect the energy levels at small scales without greatly altering pair dispersion. These were significant in GLAD but much weaker in the NCOM simulation. In addition the GLAD drifters were launched over a limited geographical area, producing few independent realizations and hence lower statistical significance. Restricting the NCOM set to pairs launched at the same locations yields very similar results, suggesting the model is for the most part capturing the observed dispersion.

## 1. Introduction

Submesoscale processes, i.e., with length scales of 0.1–10 km (Thomas et al. 2008), are believed to be important in the upper ocean (McWilliams 2008; Klein 2009). These are the transition scales between the largely balanced quasi-2D flows at the mesoscales and 3D (unbalanced) flows at smaller scales. While observational evidence of submesoscale activity in the ocean is accumulating, important questions about their dynamics and the consequences for transport remain.

In the atmosphere, the balanced scales are characterized by a kinetic energy spectrum proportional to  $k^{-3}$ , where  $k$  is the horizontal wavenumber (Nastrom and Gage 1985). The consensus is that this reflects a quasi-2D enstrophy cascade toward smaller scales (Kraichnan 1967; Charney 1971). At scales of several hundred kilometers, the spectrum transitions to a  $k^{-5/3}$  dependence. This primarily reflects diver-

gent motions (inertia–gravity waves), at scales where the Rossby number exceeds one (Callies et al. 2014). Callies and Ferrari (2013) suggest a similar situation exists in the ocean.

The slope of the energy spectrum is important for Lagrangian transport (e.g., Bennett 2006; LaCasce 2008). With a  $-5/3$  slope the dispersion of pairs of particles (or “relative dispersion”) is *local*, meaning separations between pairs of particles are dominated by eddies of comparable scales. With a  $-3$  or steeper slope the dispersion is *nonlocal* and governed by the largest eddies in the  $k^{-3}$  range. Local dispersion results in small scale “billowing,” as with smoke from a stack, while nonlocal dispersion produces filaments. Particle dispersion can thus be used to infer aspects of the energy spectrum, which can be useful in the ocean at scales below those resolved by satellite altimetry.

Hereafter we examine relative dispersion at the surface of the Gulf of Mexico (GoM). The study was motivated by the Grand Lagrangian Deployment (GLAD), which was conducted in the vicinity of the *Deepwater Horizon* (DwH) site in July 2012

\* *Corresponding author address:* Francisco J. Beron-Vera, RSMAS/ATM, University of Miami, 4600 Rickenbacker Cswy., Miami, FL 33149.  
E-mail: fberon@rsmas.miami.edu

and in which a large number of surface drifters were deployed (Olascoaga et al. 2013; Poje et al. 2014; Jacobs et al. 2014; Coelho et al. 2015). A primary goal of GLAD was to study dispersion at the submesoscales in the GoM.

Relative dispersion in the GoM has been studied previously. LaCasce and Ohlmann (2003) examined “chance pairs” of drifters (i.e., drifters not deployed together) from the Surface-CURRENT and Lagrangian drifter Program (SCULP) (Ohlmann and Niiler 2005) and found nonlocal dispersion below the deformation radius,  $L_D$ , which is approximately 45 km in the GoM (Chelton et al. 1998). Supporting evidence, using pair separation probability distribution functions (PDFs), was obtained by LaCasce (2010). However, using different measures (the second order longitudinal velocity structure function and the separation-averaged relative diffusivity) with the GLAD drifters, Poje et al. (2014) concluded the dispersion was local, from few hundred meters to several hundred kilometers, implying a shallower kinetic energy spectrum.

Relative dispersion is often studied using two types of measures (LaCasce 2008). The first treats *time* as the independent variable. This includes the relative dispersion (the mean square pair separation), the kurtosis (the normalized fourth moment) and the separation PDF. The second type uses *distance* as the independent variable. This includes the structure functions, the separation-averaged relative diffusivity and the finite-scale Lyapunov exponent (FSLE) (Artale et al. 1997; Aurell et al. 1997). The two types often produce different results, but the reasons for this are rarely examined.

In the present paper, we examine both types of statistics, using synthetic particles and drifters in the GoM. The former were obtained by integrating surface velocities produced by a data-assimilative simulation with the 1-km-resolution Navy Coastal Ocean Model (NCOM) (Jacobs et al. 2014), and the latter are the drifters in the GLAD experiment. The model allows for large numbers of particles, increasing statistical reliability, whereas the drifters more accurately reflect the actual situation in the GoM.

The paper is organized as follows. In Section 2 and Appendix A we present relevant theory for pair-separation statistics. In Section 3 we examine the NCOM pair separations, and the GLAD pairs in Section 4. A summary and concluding remarks are offered in Section 5. Details of the numerical simulation and the GLAD experiment are given in Appendices B and C, respectively.

## 2. Theory

Let  $r_0$  be the distance between two fluid parcels at time  $t = 0$  and  $r$  be the separation at time  $t$ . In homogeneous, stationary, and isotropic 2D turbulence, the PDF of pair separations,  $p(r, t)$ , obeys a Fokker–Planck equation:

$$\partial_t p = r^{-1} \partial_r (r \kappa_2 \partial_r p), \quad (1)$$

where  $\kappa_2(r)$  is the scale ( $r$ ) dependent relative diffusivity. The 3D version of (1) was proposed by Richardson (1926) to describe smoke dispersion in the atmospheric boundary layer. Richardson obtained a self-similar solution, based on an empirical diffusivity derived from observations. The equation was later derived by Kraichnan (1966) using his “abridged Lagrangian history direct interaction approximation” and by Lundgren (1981), assuming an advecting velocity with a short correlation time. For an overview, see Bennett (2006, Chapter 11).

Pair dispersion depends on whether the pair velocities are correlated or not, specifically whether the normalized Lagrangian velocity correlation

$$\frac{2\langle v_i \cdot v_j \rangle}{\langle v_i^2 \rangle + \langle v_j^2 \rangle} = 1 - \frac{\langle (v_i - v_j)^2 \rangle}{\langle v_i^2 \rangle + \langle v_j^2 \rangle} \quad (2)$$

(where the angle bracket indicates statistical average) equals 1 or 0, respectively (e.g., Koszalka et al. 2009). The second term on the right side is proportional to the second-order velocity structure function,

$$S_2(r) := \langle v^2 \rangle \equiv \langle (v_i - v_j)^2 \rangle, \quad (3)$$

where  $v$  is the difference in the Eulerian velocity between points separated by a distance  $r$ . The Eulerian–Lagrangian equivalence in (3) is a distinguishing aspect of homogeneous, isotropic turbulence (Bennett 1984).

At large separations, when the pair velocities are uncorrelated, the relative diffusivity  $\kappa_2$  is constant and equal to twice the single particle diffusivity. At smaller scales,  $\kappa_2$  can be inferred if the energy spectrum has a power law dependence, i.e.,  $E(k) \propto k^{-\alpha}$  (Bennett 1984). In either case equation (1) can then be solved (Bennett 2006). Relevant 2D solutions are given in LaCasce (2010) and Graff et al. (2015), and are reproduced in Appendix A. From these, the (raw) statistical moments, given by

$$\langle r^n \rangle := 2\pi \int_0^\infty r^{n+1} p(r, t) dr, \quad (4)$$

can be calculated. Table 1 shows the time dependences for  $\langle r^2 \rangle$  (the relative dispersion) and the  $\langle r^4 \rangle / \langle r^2 \rangle^2$  (kurtosis) in the three specific 2D dispersion regimes considered here.

TABLE 1. The pair-separation measures in the three regimes considered here. The measures are the kinetic energy spectrum,  $E(k)$ , where  $k$  is wavenumber; the two particle diffusivity,  $\kappa_2(r)$ , where  $r$  denotes separation; the second-order longitudinal structure function,  $S_2(r)$ ; the relative dispersion,  $\langle r^2 \rangle$ ; and the separation kurtosis,  $\langle r^4 \rangle / \langle r^2 \rangle^2$ . The latter two are based on the (raw) statistical moments of the time-dependent probability distribution function (PDF) of pair separations, obeying (1). The results shown for the Richardson and Rayleigh cases are the asymptotic (long time) limits.

	Lundgren	Richardson	Rayleigh
$E(k)$	$\propto k^{-3}$	$\propto k^{-5/3}$	–
$\kappa_2(r)$	$= r^2/T$	$= \beta r^4/3$	$= \text{const}$
$S_2(r)$	$\propto r^2$	$\propto r^{2/3}$	$= \text{const}$
$\langle r^2 \rangle$	$= r_0^2 e^{8t/T}$	$\sim 5.2675\beta^3 t^3$	$\sim 4\kappa_2 t$
$\langle r^4 \rangle / \langle r^2 \rangle^2$	$= e^{8t/T}$	$\sim 5.6$	$\sim 2$

The nonlocal regime [which we refer to as the “Lundgren regime,” after Lundgren (1981)] corresponds to an energy spectrum at least as steep as  $k^{-3}$ , with a structure function  $S_2 \propto r^2$ . The PDF is not self-similar, but rather becomes more and more peaked. Both the dispersion and kurtosis increase exponentially in time. The local regime we will consider has a Kolmogorov energy spectrum,  $E \propto k^{-5/3}$ , or equivalently  $S_2 \propto r^{2/3}$ , and referred as the “Richardson regime” after Richardson (1926). In this case the separation PDF asymptotes to a self-similar form, with a kurtosis of 5.6, and the dispersion increases as time cubed. With uncorrelated pair velocities, the second-order structure function is constant with separation (and equal to twice the mean square single particle velocity). The PDF also asymptotes to a self-similar form, with kurtosis of 2 and the dispersion increasing linearly in time. This self-similar PDF is a Rayleigh distribution, so we refer to this as the “Rayleigh regime.”

### 3. Simulated pair-separation statistics

The simulated trajectories were constructed by integrating surface velocities produced by an NCOM simulation (cf. Appendix B). The integrations were carried out using a stepsize-adapting fourth/fifth-order Runge–Kutta method with interpolations obtained using a cubic scheme. One-month-long records, with 10 positions per day, were produced with a range of initial separations, from the smallest scale resolved by the model simulation up to 30 km ( $r_0 = 1, 5, 10$  and 30 km). The trajectories were initiated every other day in the northern GoM near the DwH site, in two  $5 \times 5$  100-km-width grids displaced

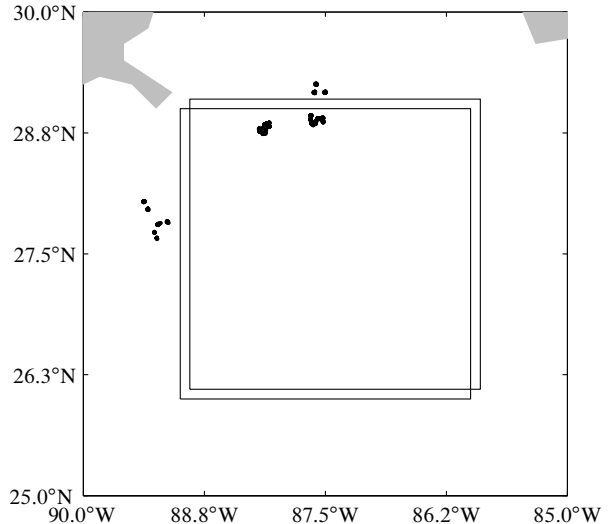


FIG. 1. The rectangles indicate the boundaries of the grids of initial positions for the integration of trajectory pairs (with  $r_0 = 1$  km initial separation) using surface velocities produced by the 1-km-resolution Navy Coastal Ocean Model (NCOM) simulation of the Gulf of Mexico (GoM). Dots indicate deployment locations of drifters from the Grand Lagrangian Deployment (GLAD).

by the chosen separation. The reference and auxiliary grids with  $r_0 = 1$  km are shown in Fig. 1. The trajectories were started 1 July 2013 and 1 February 2014 to survey summer and winter conditions. The two were expected to exhibit different pair-separation statistics, as the mixed layer is deeper in winter.

However, snapshots of the instantaneous surface vorticity (Fig. 2) reveal roughly the same range of eddy scales in the two seasons. The results seen hereafter similarly show only small changes with season. These figures also reveal that the West Florida Shelf and the Bay of Campeche are relatively eddy inactive regions, and that an anticyclonic ring has pinched off from the Loop Current. Apart from these regions however the eddy field does not exhibit significant spatial variability. Thus we assume homogeneity holds fairly well, as assumed in Section 2.

An additional theoretical prerequisite is stationarity. While temporal variability of the simulated background eddy field is evident, this mainly manifests on seasonal timescales. Therefore, considering motion over a period of 1 month, as we do here, is not restrictive but rather necessary for stationarity to be fairly well guaranteed.

Isotropy, the remaining prerequisite, is also realized. This can be seen by plotting the ratio of the zonal to the meridional relative dispersion ratio as a function of scale (Morel and Larcheveque 1974), as shown in Fig. 3. Isotropy holds in both summer

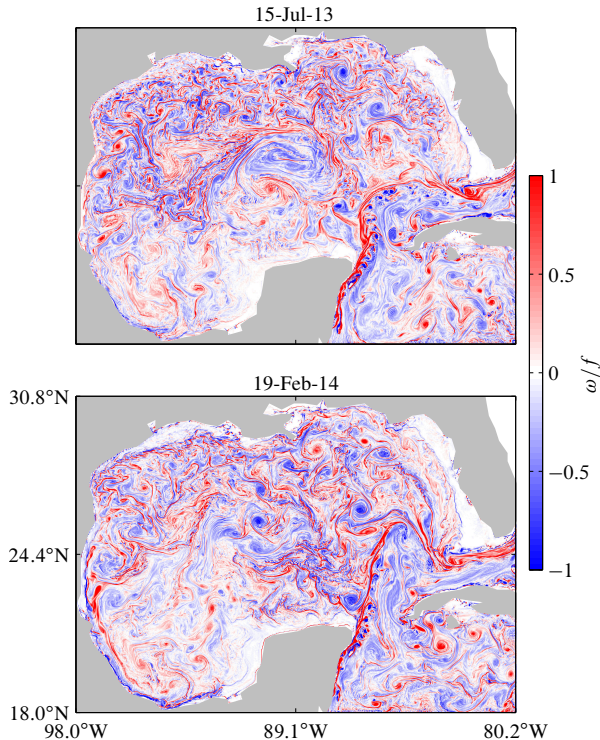


FIG. 2. Snapshots of surface vorticity (normalized by the mean Coriolis parameter in the GoM) from the NCOM simulation in summer (top) and winter (bottom).

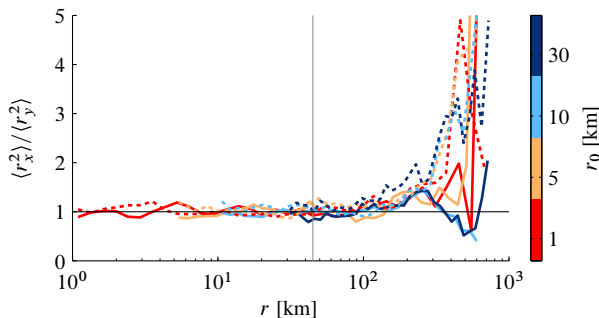


FIG. 3. Zonal-to-meridional relative dispersion ratio as a function of pair separation in summer (solid) and winter (dashed) based on simulated trajectory pairs with various initial separations. The vertical line indicates the gravest baroclinic Rossby deformation radius.

(solid) and winter (dashed), irrespective of the initial pair separation. At separations exceeding 100 km, the dispersion becomes zonally anisotropic, as it does in the atmosphere (Graff et al. 2015). But below that, the dispersion is isotropic.

We then determine over which scales the pair motion is correlated. Inspection of Fig. 4 reveals that, fairly insensitive to the initial pair separation, the motion is correlated below the deformation radius,

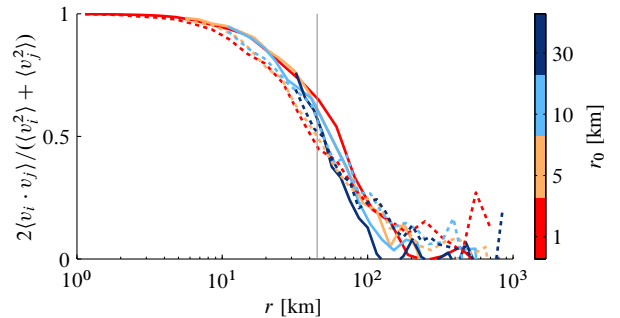


FIG. 4. The normalized Lagrangian velocity correlation as function of scale in summer (solid) and winter (dashed) for various initial separations in the NCOM simulation. The vertical line indicates the Rossby deformation radius.

in both seasons. At  $L_D$ , the correlation is roughly 0.5. The motion is strongly correlated below 20 km and decorrelated above 100 km. Thus the proper framework for interpretation above 100 km is absolute dispersion, possibly with the inclusion of a mean zonal shear.

We now inspect the pair separation PDFs and compare them to the theoretical predictions (Fig. 5). We calculated the PDFs using kernel density estimation as implemented in Matlab’s function `ksdensity` with positive support. Each theoretical PDF has two parameters: the initial separation,  $r_0$ , and a growth parameter. Since all pairs have the same initial separation, we assume  $r_0$  is the same as in the simulation. The growth parameters for the Lundgren and Richardson distributions ( $T$  and  $\beta$ , respectively) were determined by fitting the dispersion using least squares during the initial period, up to the point when the root-mean-squared (rms) separation was a factor  $a$  greater than the initial value. We chose  $a = 5$ , but the results are fairly insensitive to the choice. The parameter for the Rayleigh PDF ( $\kappa_2$ ) was calculated from the relative dispersion at late times, after the pair motion was decorrelated, as described in Appendix A.

The PDFs are plotted with the theoretical curves at  $t = 3.5$  d. Several initial separations are used, for particles deployed in summer (in red) and winter (in blue), and the parameters obtained for the theoretical curves are indicated in the inserts. The observed and theoretical PDFs were compared using the Kolmogorov–Smirnov (KS) statistic (cf., e.g., Press et al. 2007); since the winter and summer distributions are so similar, we used the summer PDF for this. The degrees of freedom for the KS test are determined by the number of independent pairs. The pairs were deployed every 2 d and 100-km apart in the present simulation, so we can safely treat all pairs

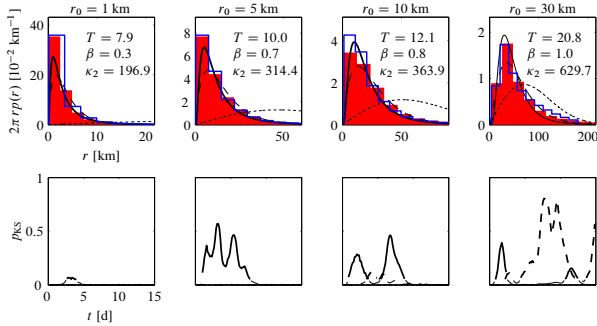


FIG. 5. (top) Pair separation probability distribution functions (PDFs) in summer (red) and winter (blue) for various initial separations. The PDFs are shown at time  $t = 3.5$  d. Solid and dashed, and dot-dashed curves are theoretical PDFs in the Lundgren, Richardson, and Rayleigh regimes, respectively. Parameters  $T$  (with units  $\text{d}^{-1}$ ) and  $\beta$  (with units  $\text{km}^{2/3} \text{d}^{-1}$ ) for the Lundgren and Richardson PDFs, respectively, were obtained by comparing the theoretical and observed dispersion curves via least squares out to the time by which  $\sqrt{\langle r^2 \rangle} = 5r_0$ . The relative diffusivity  $\kappa_2$  (with units  $\text{km}^2 \text{d}^{-1}$ ) for the Rayleigh distribution was calculated as the mean of the relative dispersion divided by  $4t$  after  $t = 10$  d (Appendix A). When a theoretical curve is statistically similar to the observed PDF in summer at the 95% confidence level, it is drawn in bold. (bottom) The Kolmogorov-Smirnov probability for the theoretical curves vs the summer PDF as a function of time.

as independent. In the figure, the bold curve is statistically similar to the observed summer PDF, with 95% confidence. The lower panels show how the KS probability evolves with time, over the first 15 days. When a curve exceeds 0.05, it is plotted in bold.

Consider the case with  $r_0 = 1$  km initial separation. The summer and winter PDFs are very similar and are highly kurtosed, with most pairs having small separations but some having much larger ones. The Lundgren distribution (solid) has a similar shape, and indeed is statistically the same at the 95% confidence level. In contrast, the Richardson (long-dashed) and Rayleigh (short-dashed) distributions have a shorter tail and much larger mode, respectively. The KS probability (lower panel) though suggests the Lundgren PDF is significantly similar only during a brief period, near  $t = 3$  d.

The results with  $r_0 = 5$  and  $10$  km are similar, in that observed PDFs resemble the Lundgren distribution. The similarity moreover is significant at the 95% level for much of the first 10 d. The Richardson PDF on the other hand is not similar over the same period. With  $r_0 = 30$  km, the PDF is statistically similar to the Lundgren only briefly, but then resembles the Richardson. However, recall that 30 km is only slightly less than the deformation radius, when the pair velocities are significantly decorrelated. We

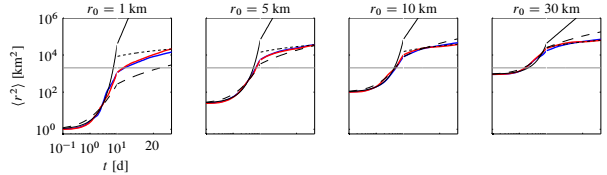


FIG. 6. Relative dispersion (second moment of the pair-separation PDF) in summer (red) and winter (blue) for the NCOM pairs with various initial separations. The Lundgren and Richardson predictions are indicated in solid and long-dashed curves, respectively. The short-dashed line is the long-time asymptotic Rayleigh relative dispersion. The horizontal dashed line indicates the deformation radius. Note that the  $t$ -axis is logarithmic until  $t = 10$  d and linear thereafter.

do not find similarity with the Rayleigh distribution in any case, during these initial 15 d.

The relative dispersion curves are shown in Fig. 6. The winter (red) and summer (blue) curves are nearly identical, again supporting similar behavior in the two seasons. The initial growth is close to exponential initially, with an e-folding time on the order of 1 d. The exception is the  $r_0 = 30$  km case, where the separations are only briefly below the deformation radius (indicated by the horizontal line). With the two larger initial separations, the late dispersion increases linearly, in line with diffusive growth, but this is not apparent in the 1 and 5 km cases. There is a clear suggestion of Richardson-like growth with  $r_0 = 10$  km, but in the other cases the dispersion is either greater or less than this.

Being the fourth moment of the PDF, the kurtosis (Fig. 7) is more sensitive to the tails of the distribution. With the smallest initial separation ( $r_0 = 1$  km), the kurtosis grows rapidly, reaching values greater than 20, in both seasons. Under non-local dispersion the kurtosis grows exponentially and at the same rate as the dispersion (Table 1). The observed growth is roughly consistent with this, with an e-folding time of roughly 1 d. With  $r_0 = 5$  km, the initial growth is curtailed and the maximum values obtained are less. With  $r_0 = 10$  and  $30$  km, the kurtosis quickly relaxes toward 2, the asymptotic limit for the Rayleigh distribution. There is little support for a Richardson regime here; the kurtosis exceeds the asymptotic limit of 5.6 at the smallest separations and falls below that at the larger separations.

The velocity structure functions ( $S_2$ ) are shown in Fig. 8 for summer (solid) and winter (dashed) pairs. These are very similar, flattening out at scales exceeding 100 km, as expected for uncorrelated motion. With  $r_0 = 1$  km,  $S_2$  exhibits the  $r^2$  dependence expected in a nonlocal regime at the smallest separations. With larger  $r_0$  the curves do not have a unique power-law-dependence but suggest instead

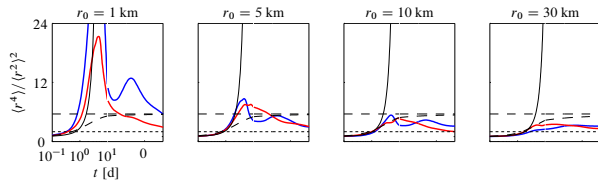


FIG. 7. Kurtosis (normalized fourth moment of the pair-separation PDF) in summer (red) and winter (blue) for the NCOM pairs with various initial separations. The Lundgren and Richardson curves are indicated by the solid and long dashed curves, respectively. Parameter-independent long-time asymptotic limits in the Rayleigh and Richardson regimes are indicated by the short- and long-dashed horizontal lines. As in the previous figure, the  $t$ -axis is logarithmic until  $t = 10$  d and linear thereafter.

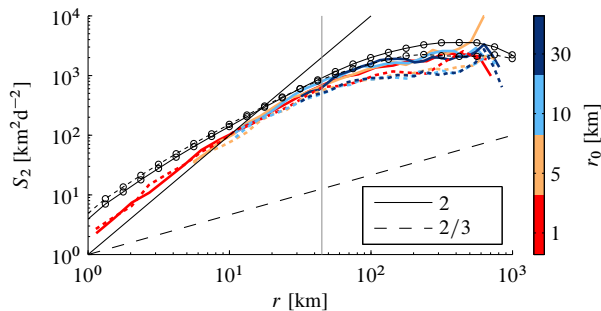


FIG. 8. Second order structure functions in summer (solid) and winter (dashed). Colored curves are Lagrangian estimates for different initial separations. The curves with circles are Eulerian estimates. Solid and dashed straight lines have structure function slopes (indicated) in the theoretical Lundgren and Richardson regimes, respectively. The vertical line indicates the Rossby deformation radius.

a transition between the  $r^2$  and  $r^0$  asymptotic limits. We also calculated the Eulerian  $S_2$  using velocity time series at fixed positions (curves with circles), and this mirrors the Lagrangian  $S_2$  well, supporting the assumptions of homogeneity and isotropy.

Thus both the time- and distance-averaged measures indicate nonlocal dispersion at the smallest separations and uncorrelated motion above 100 km. There was some suggestion of an intermediate Richardson regime (primarily in the dispersion), but the kurtoses and structure functions imply these scales are rather a transition between the small and large scale limits.

One wonders of course to what extent numerical dissipation in the model is responsible for the nonlocal dispersion at the smallest scales. So we turn to the GLAD drifters, which are not so affected.

#### 4. Observed pair-separation statistics

The GLAD pairs were obtained from quarter-hourly drifter positions from the GLAD experiment

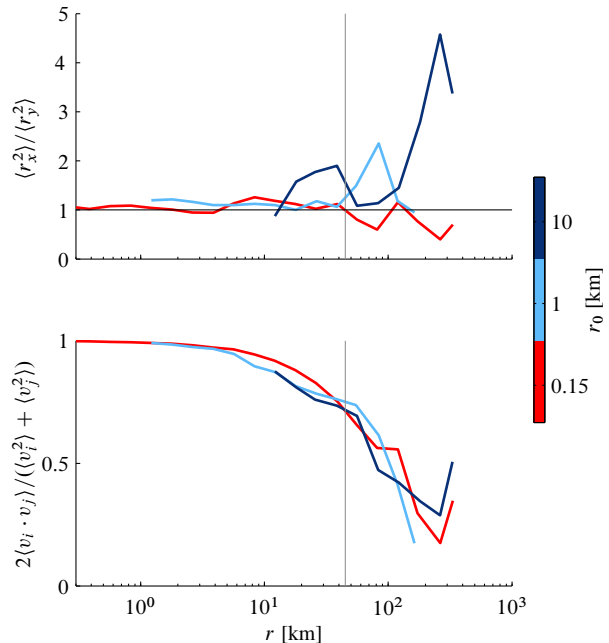


FIG. 9. As in Figs. 3 (top) and 4 (bottom) but based on GLAD trajectory pairs in three initial separation classes.

(cf. Appendix C). The drifters were deployed near the DwH site, as indicated by the black dots in Fig. 1. Various initial separation classes were identified:  $r_0 \approx 0.15$ , 1, and 10 km. A total of 132, 127, and 276 original pairs were obtained in each class.<sup>1</sup> As in Poje et al. (2014), we consider trajectory records spanning the initial 25 d after deployment, to avoid enhanced windage effects on the drifters during the passage of hurricane *Issac*.

As the trajectories span no more than one month, we assume stationarity holds. Homogeneity cannot be determined with the available data, but the NCOM results suggest this is not an unreasonable assumption. Isotropy is found for separations less than about 100 km or so (Fig. 9, top panel). Furthermore, the pair velocities are correlated over the isotropic scales, with correlations falling below 0.5 above 100 km (Fig. 9, bottom panel).

The time-based statistics are shown in Fig. 10. The parameters for the theoretical curves were obtained as before, by matching the observed dispersion from the initial separation up to the scale at which the rms separation  $\sqrt{\langle r^2 \rangle} = 5r_0$ . In principle one could also treat the initial separation as a free parameter, since a range of initial values is present, but we chose to set  $r_0$  equal to the mean value for the drifters in each chosen range.

<sup>1</sup>The specific initial separation ranges are:  $0.12 \text{ km} < r_0 < 0.19 \text{ km}$ ,  $0.84 \text{ km} < r_0 < 1.19 \text{ km}$ , and  $9.85 \text{ km} < r_0 < 10.19 \text{ km}$ .

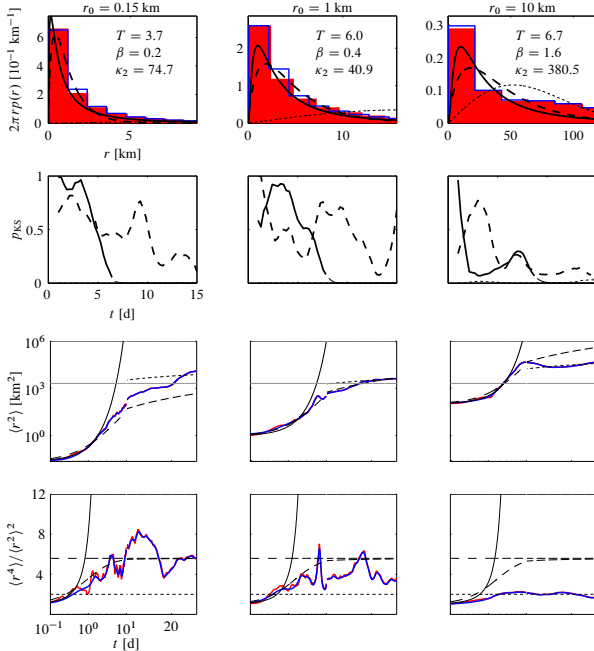


FIG. 10. As in Figs. 5 (first and second rows), 7 (third row), and 6 (fourth row) but for separations experienced by the raw (red) and lowpass-filtered (blue) GLAD trajectory pairs. The cut-off period for the filter is 2.5 d.

The GLAD PDFs 3-d after deployment are shown in red in the top panels of Fig. 10 for the 3 initial separations above. The PDFs are somewhat coarser than for the synthetic particles as there are fewer pairs, but they too are peaked at the smallest separations and exhibit extended wings.

Again, assessing the differences with the theoretical PDFs requires knowing the number of degrees of freedom, i.e., the number of independent realizations. However this number was fairly small for the GLAD experiment, as the deployment was made over a limited geographical area. Drifter clusters were deployed very near one another, so that the distance between different clusters was often much less than the putative energy-containing eddy scale of 100 km. As such, many of the pair trajectories are similar.

In fact the trajectories can be grouped into 6 classes, as shown in Fig. 11. The numbers of pairs ( $N$ ) in each group are indicated in the inserts, and these range from 13 to 29. As most of the drifters in each group were deployed on a single day, these obviously should not be considered as independent realizations. The exception was the  $N = 17$  group, which were launched on two different days. Thus the number of independent realizations here is only 7, 1 for each class and 2 for the  $N = 17$  group. However, allowing for some variation in each group, we esti-

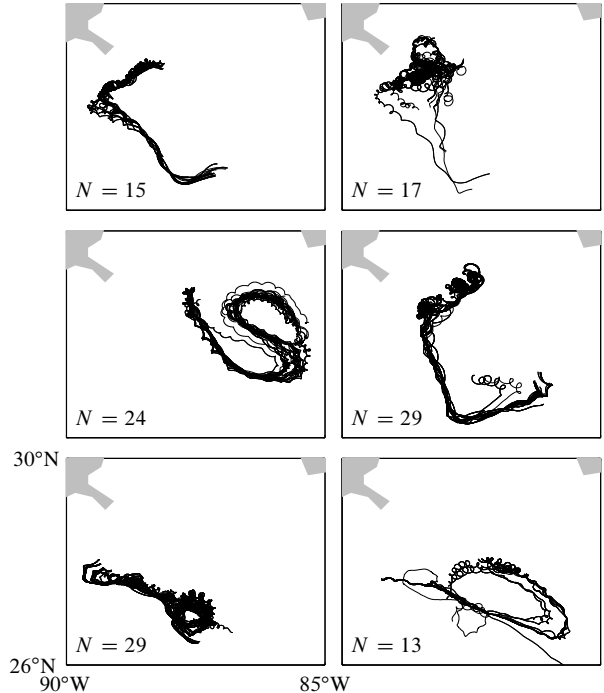


FIG. 11. GLAD trajectory pairs with initial separation  $r_0 \approx 1$  km arranged into groups exhibiting similar behavior. The number ( $N$ ) of pairs in each group is indicated.

ated the degrees of freedom as 3 times this, or 21. As such, we effectively treat each group as a triplet of drifters.

With so few degrees of freedom, one cannot distinguish the theoretical curves at the 95% confidence level. Thus both the Lundgren and Richardson PDFs are statistically similar over the initial 10 d, with all three separations. Only the Rayleigh distribution can be excluded during this period.

The relative dispersion is indicated by the red curves in the third row of panels in Fig. 10 (the curves are often obscured by blue curves indicating the dispersion for a lowpass filtered data set, discussed hereafter). The dispersion with the smallest initial separation is close to exponential initially but increases more slowly after  $t = 2$  d. With  $r_0 = 1$  km however the dispersion follows the Richardson prediction over much of the first 20 d. With this separation and  $r_0 = 10$  km, the dispersion asymptotes to linear growth at late times.

The kurtoses are plotted in red in the bottom panels of Fig. 10. With  $r_0 = 0.15$  km the kurtosis grows and then oscillates around the Richardson asymptotic limit of 5.6. With  $r_0 = 1$  km, the kurtosis increases more slowly, lying between the asymptotic limits for the Richardson and Rayleigh regimes, while

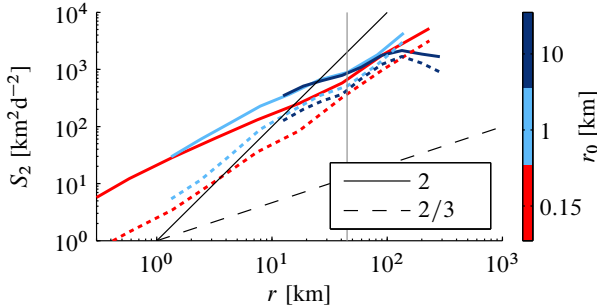


FIG. 12. As in Fig. 8 but using raw (solid) and lowpassed (dashed) GLAD trajectory pairs.

the kurtosis is close to the latter limit for most of the period with  $r_0 = 10$  km.

The second-order structure functions (Fig. 12, solid curves) on the other hand are clearly suggestive of a Richardson regime. With the  $r_0 = 0.15$  km pairs, the curve exhibits a power-law-dependence near  $r^{2/3}$  from the smallest scales to roughly 200 km, consistent with the results of Poje et al. (2014). However, with  $r_0 = 10$  km a plateau is observed above 100 km, in agreement with the motion being largely uncorrelated at those scales.

Thus the GLAD results are ambiguous. The PDFs are inconclusive, due to having too few degrees of freedom. The dispersion curves suggest nonlocal dispersion at small scales while the kurtosis and the structure functions are more consistent with a Richardson regime. What causes these differences among the measures, and are the results actually different than those from the synthetic pairs?

#### a. Inertial oscillations

One important difference can be seen in the trajectories themselves (Fig. 11). Many of the GLAD drifters experience inertial oscillations: anticyclonic loops with a period near 1 d (the local inertial period) (cf., e.g., Gill 1982). Frequency spectra of the individual velocities, as in the example in Fig. 13, exhibit a significant peak at the inertial period (right). Except for this, the energy resides primarily at the lowest frequencies. Consistently, the trajectory (left) exhibits anticyclonic loops superimposed on a larger scale structure.

While inertial oscillations have a narrow frequency spectrum [unless modified by background rotation (e.g., Kunze 1985)], the Lagrangian motion possesses a range of spatial scales. These are determined by the particle velocity, with faster-moving particles executing larger loops. So the spectral profile in wavenumber space is broader; as such, the oscillations could potentially influence the separation statistics.

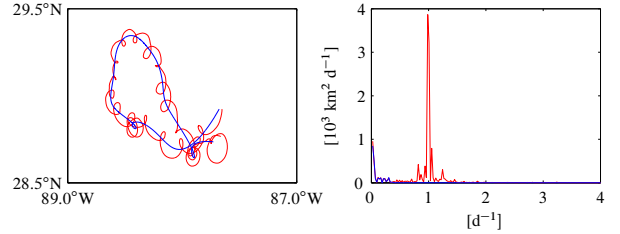


FIG. 13. (left) Raw (red) and lowpassed (blue) GLAD drifter trajectory. (right) Corresponding zonal velocity power spectra.

To test this, we applied a lowpass filter to remove the inertial oscillations.<sup>2</sup> The resulting spectrum and the corresponding trajectory are shown in blue in Fig. 13. The filter eliminates the peak near the inertial frequency while preserving the larger meandering motion.

Lowpass filtering has relatively little effect on the time-based dispersion measures. The blue curves in Fig. 10 correspond to the filtered GLAD trajectories, and in all cases these mirror the results for the unfiltered trajectories. This is because the inertial oscillations on nearby drifters are very similar (see below) and thus do not greatly alter their separation. Moreover, as the drifters return approximately to their previous positions every inertial period, the net effect is small.

The impact on the velocity structure function however is greater (Fig. 12). With the lowpass filter (dashed curves), the energy at small scales is reduced and the structure function increases faster than  $r^{2/3}$ .

Inertial oscillations are only weakly captured in the NCOM simulation, so this effect is missed in the synthetic trajectories, which are furthermore computed from daily velocities. To test how they would have altered the statistics, we *added* inertial oscillations to the NCOM trajectories. This was done by modifying the  $i \neq j$  positions as

$$x_i(t) \mapsto x_i(t) + A(\sin \omega t, \cos \omega t - 1) \quad (5)$$

$$x_j(t) \mapsto x_j(t) + (A + B(r_{ij}))(\sin \omega t, \cos \omega t - 1). \quad (6)$$

Here  $2\pi/\omega = 1$  d, roughly equal to the local inertial period. The amplitude,  $A$ , was taken to be a random number varying over the range of observed loop amplitudes. The amplitude  $B(r_{ij}(t))$  represents the growing difference between amplitudes on nearby drifters.

The latter was chosen to mimic the behavior of the GLAD pairs. The inertial wave scale is generally much larger than the smallest pair separations here

<sup>2</sup>The filter was a sixth-order lowpass Butterworth filter with  $2.5 \text{ d}^{-1}$  cut-off frequency.

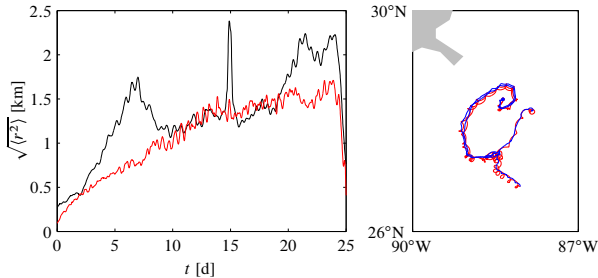


FIG. 14. (left) The root-mean-squared (rms) separation for highpass-filtered GLAD trajectory pairs (black) plotted against the rms separation of the lowpass-filtered trajectories. The red curve is an empirical fit used to determine the difference in amplitude of the artificial near-inertial oscillations imposed on the NCOM trajectories. The GLAD trajectories belong to the  $r_0 \approx 1$  km initial separation class and the NCOM trajectories start at GLAD positions. (right) An example of an NCOM pair, without (blue) and with (red) the near-inertial oscillations superimposed.

(e.g., Webster 1968; Pollard 1980; Young and Jelloul 1997; Chant 2001). Consistently, the high-passed pair velocities decorrelate on scales comparable to those of the full velocities (not shown), indicating scales of at least 100 km. As the pair velocities are similar for nearby drifters, the loops are correlated and similarly large. But as the drifters separate, the difference in loop amplitude grows as the velocity difference grows. To gauge this, we calculated the rms difference in the highpass filtered pair separation and plotted it against the rms pair separation, determined from the lowpass filtered trajectories. This is shown in black in the left panel of Fig. 14. The rms difference is roughly 0.5 km initially and increases to a value near 2 km at separations greater than 20 km.

Choosing  $B(r_{ij}(t)) = B_0 \sqrt[4]{r_{ij}(t)/r_0}$  with  $B_0 = 3/4$  yields the separation curve shown in red. This mimics the observed growth fairly well. The effect of the addition on a single pair is shown in the right panel, with the modified trajectories exhibiting anti-cyclonic loops.

The effect on the synthetic particle statistics is seen in the middle panels of Fig. 15. These are for a set of NCOM trajectories initiated at the GLAD launch positions, with  $r_0 = 1$  km. The blue curves are for the unmodified trajectories and the red have the inertial oscillations superimposed. The PDFs, relative dispersion, and kurtosis are almost unaffected by the addition of the oscillations. But the structure function is significantly altered, with that for the modified trajectories exhibiting more energy at subdeformation scales. While  $S_2$  increases as  $r^2$  for the original trajectories, the dependence for the modified set is nearer  $r^{2/3}$ .

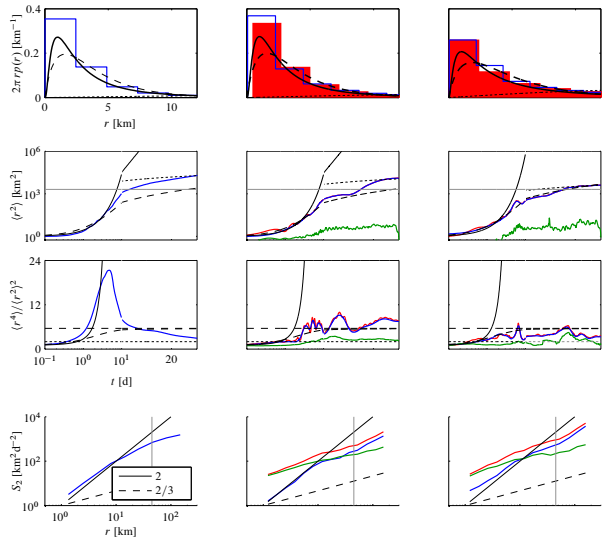


FIG. 15. Separation PDFs (top), relative dispersion (second row), kurtosis (third row), and velocity structure function (bottom) for: NCOM pairs at  $r_0 = 1$  km separation, as shown in Figs. 5–8, for comparison (left); NCOM trajectories started from the GLAD positions with  $r_0 \approx 1$  km (middle); and actual GLAD trajectories with  $r_0 \approx 1$  km (right). In blue are results based on NCOM trajectories or lowpassed GLAD trajectories. In red are results based on NCOM trajectories with near-inertial oscillations superimposed or raw GLAD trajectories. In green are results based on highpassed trajectories.

Shown in green are the statistics for the inertial oscillations alone, obtained from the trajectories following highpass filtering (with a cut-off of 2.5 d). These show that the contributions to the dispersion and kurtosis from the inertial oscillations are much less than from the low frequency components. But below separations of roughly 20 km, the inertial component dominates the second order structure function.

We find that adding the oscillations affects other distance-based measures as well, such as the relative diffusivity and the FSLE (not shown). But as they do not significantly alter the time-based metrics, they cannot explain the other differences between the GLAD and NCOM statistics.

### b. Sampling

The second factor influencing the GLAD results is the sampling strategy alluded to earlier. Most of the GLAD pairs were deployed very near one another and behaved similarly. This reduced the effective degrees of freedom, and the mesoscale dispersion was not captured well.

The effect can be assessed by comparing in Fig. 15 the statistics for the  $r_0 = 1$  km NCOM pairs deployed at the GLAD locations (middle) with those from

the full NCOM deployment (left) and the GLAD set (right). The statistics for the reduced NCOM set are strikingly similar to those from GLAD, both the time- and the distance-based measures. The kurtoses are somewhat lower with the GLAD drifters, and the transition scale below which the structure function from the highpassed velocities crosses that from the lowpassed velocities is smaller (10 vs 20 km). But the addition or removal of inertial oscillations otherwise affects the trajectories in the same ways. And the results from both sets differ markedly from those for the full NCOM set.

This implies the differences between the GLAD statistics and those of the full NCOM set may be due to sampling rather than to dynamics. With identical sampling, the NCOM model gives an accurate representation of the dispersion and the structure function. This is remarkable, given that the model resolution is only 1 km. The reason however can be inferred from the frequency spectrum in Fig. 13: except for the peak at the inertial frequency, the spectrum is dominated by low frequency motions. It is these motions, due to mesoscale features, which dominate the pair dispersion, and these are captured by the model. This is the essence of nonlocal dispersion—it is controlled by structures with larger scales and lower frequencies.

## 5. Summary and concluding remarks

We have investigated the dispersion experienced by simulated and observed pairs initiated near the *Deepwater Horizon* (DwH) site in the northern Gulf of Mexico (GoM). The simulated separations were produced using synthetic pairs advected by surface velocities from a data-assimilative Navy Coastal Ocean Model (NCOM) simulation, with an effective horizontal resolution of 1 km, during July 2013 and February 2014. The observed separations come from drifter pairs from the Grand Lagrangian Deployment (GLAD), conducted in July 2012. The investigation involved various statistical descriptors, namely, the probability distribution function (PDF) of pair separations, its second moment (relative dispersion), its fourth moment (kurtosis), and the (second-order) velocity structure function.

The measures are consistent for the NCOM pairs, suggesting nonlocal dispersion at the smallest separations and diffusive dispersion at separations greater than 100 km, where the pair velocities are decorrelated. Similar results were obtained in both winter and summer seasons. The results were more ambiguous with the GLAD pairs. While the pair motion is also uncorrelated at scales exceeding 100 km, the dispersion regime cannot be distinguished from the

PDFs, dispersion or kurtosis. The structure functions on the other hand indicate Richardson dispersion from the smallest scales to beyond the decorrelation scale.

Two effects impact the GLAD results. With such high temporal resolution (10-min sampling), the drifters resolve inertial oscillations. These energetic motions however only weakly affect pair dispersion. The size of the loops depend on the drifter velocity (e.g., Gill 1982), and since nearby drifters have nearly the same velocity, the size of the loops is nearly the same initially. As the pair separates however, the velocity difference grows and the amplitude difference increases. However, as the drifters return approximately to their starting position after an inertial period, the net effect on the separation during that time is small. As such, the effect is greatly overwhelmed by mesoscale stirring.

The oscillations do however alter distance-averaged measures. The velocity structure function is one such measure, and this is dominated by inertial oscillations below roughly 10 km. Filtering the trajectories to remove the inertial oscillations steepens the structure functions without affecting the time-based measures. Likewise, adding inertial oscillations to the trajectories from the model, which has weak inertial variability, causes the structure function to shallow, lending the appearance of local dispersion.

The second effect concerns the sampling in GLAD. As the goal was to resolve submesoscale dispersion in the region, the drifters were deployed in several tight clusters. As these spanned scales much less than the correlation length scale (100 km), the pairs behaved similarly. We found the drifters could be separated into 6 distinct classes, each displaying a characteristic path. This reduced the degrees of freedom and led effectively to an undersampling of the mesoscale stirring. Using synthetic particles deployed at the same locations yielded nearly identical, and equally ambiguous, dispersion statistics.

The conclusion is that the 1-km model likely captures the dispersion in the GLAD experiment over the sampled scales. This argues in favor of nonlocal dispersion, because the stirring is dominated by large scale, low frequency motions which are well-resolved by the model. It also supports using altimeter-derived geostrophic velocities to study dispersion here, as the dominant eddies are marginally resolved by altimetry. Olascoaga et al. (2013) suggested the mesoscale circulation dominates in shaping the patterns formed by drifters in the GLAD experiment, and the present results are consistent with this.

Previously, LaCasce and Ohlmann (2003) observed exponential dispersion among “chance pairs” from the Surface-CURRENT and Lagrangian drifter Program (SCULP), from separations of 1 km up to  $L_D$  ( $\approx 50$  km). The SCULP pairs exhibited an e-folding time on the order of 1 d, similar to the time scales inferred here, and exhibited large kurtoses. LaCasce (2010) found moreover that the SCULP PDFs resemble the Lundgren distribution. Note the SCULP drifters had daily positions and so were essentially devoid of inertial oscillations. LaCasce and Ohlmann (2003) did not observe diffusive dispersion at super-deformation scales but something closer to ballistic growth, with the dispersion increasing as  $t^{2.2}$ . Given that the pair motion is uncorrelated above  $L_D$ , such growth most likely reflects shear dispersion, due to a large scale flow. Indeed, many of the SCULP drifters were advected by boundary currents.

Poje et al. (2014) presented the first analysis of the GLAD pair trajectories and concluded the dispersion was consistent with the Richardson regime, from the smallest sampled scale (0.1 km) to several hundred kilometers. However, their conclusions were based solely on distance-based measures (the second order structure function and the relative diffusivity) which are affected by inertial oscillations. It should be emphasized too that a turbulence framework cannot be applied to interpret results at separations of hundreds of kilometers, as the pair velocities are uncorrelated.

Jullien et al. (1999) and Jullien (2003) calculated separation PDFs from pairs of particles deployed in 2D turbulent flows in the laboratory. They suggested that the separation PDF could be fit with an empirical function of the form:

$$p(r, t) = \frac{a}{2\pi\sigma r} \exp\left(-b\sqrt{\frac{r}{\sigma}}\right), \quad (7)$$

where  $\sigma = \langle r^2 \rangle^{1/2}$ , and  $a$  and  $b$  are constants. They claimed that the same PDF applied for *both* the energy and enstrophy cascade ranges, with slightly different values of  $a$  and  $b$ .<sup>3</sup> It is straightforward to show that the kurtosis for this empirical PDF (7) is:

$$\frac{\langle r^4 \rangle}{\langle r^2 \rangle^2} = \frac{9!}{5!^2} = 25.2. \quad (8)$$

There is no indication of such a large asymptotic limit in either the simulated trajectories or the GLAD data. So we can most likely rule out this type of dispersion.

The present results serve as a cautionary note on using relative dispersion to deduce kinetic energy

spectra. The inertial oscillations contribute to the spectra but do not greatly impact dispersion. So finding exponential relative dispersion does not necessarily imply steep spectra. Conversely, having shallower spectra at small scales, as in the atmosphere (Nastrom and Gage 1985) and ocean (Callies and Ferrari 2013), does not rule out nonlocal pair dispersion.

It is also worth noting that the submesoscale spectrum here exhibits a scale separation. The Lagrangian frequency spectra has peaks at low frequencies and at the inertial frequency, with little energy in between. So it is possible to partition the flow into mesoscale turbulence and inertial oscillations. If instead an inverse energy cascade were occurring from the submesoscales, the intermediate scales and frequencies would be energetic.

The results also have implications for the design of dispersion experiments. Care should be taken to ensure sufficient sampling at scales exceeding those of the energy-containing eddies. Otherwise one might obtain many similar pair trajectories, with a corresponding loss of statistical confidence.

*Acknowledgments.* We thank Angelique Haza, Tamay Özgökmen, and Andrew Poje for discussions on pair-separation statistics and Jonathan Lilly on inertial oscillations. We are also grateful to three anonymous reviewers, whose comments led to significant improvements in the manuscript. The GLAD trajectory pairs were kindly identified by Angelique, who independently computed kurtosis in the several initial separation classes considered here. The GLAD drifter trajectory dataset is publicly available through the Gulf of Mexico Research Initiative Information & Data Cooperative (GRIIDC) at <https://data.gulfresearchinitiative.org> (DOI:10.7266, N7VD6WC8). The NCOM simulation was produced at the Naval Research Laboratory and can be obtained from <http://dx.doi.org/10.7266/N7FQ9TJ6>, [N76Q1V5G](http://dx.doi.org/10.7266/N76Q1V5G), and [N72Z13F4](http://dx.doi.org/10.7266/N72Z13F4). The work was supported by the Gulf of Mexico Research Initiative (FJBV) and under grant 221780 from the Norwegian Research Council (JHL).

## APPENDIX A

### PDF solutions

Solutions to the Fokker-Planck equation (1) have been derived for the turbulent inertial ranges. These assume that all pairs have the same initial separation, so that  $p(r, 0) = (2\pi r)^{-1} \delta(r - r_0)$ . Note that  $p$  is normalized, i.e.,  $\langle r^0 \rangle = 1$ . As noted, the solutions can be obtained via the Laplace transform.

<sup>3</sup>The PDF they proposed was not properly normalized. Doing so yields  $a = b^2/2$ .

A scale-independent diffusivity  $\kappa_2 = \text{const}$  occurs when the pair motion is uncorrelated. One- and two-particle statistics coincide in such a case, which is consistent with  $S_2 = \text{const}$  (indeed,  $\langle (v_i - v_j)^2 \rangle = 2\langle v_i^2 \rangle$ , which does not depend on scale). The solution to (1) is given by

$$p(r, t) = \frac{1}{4\pi\kappa_2 t} I_0 \left( \frac{r_0 r}{2\kappa_2 t} \right) \exp \left( -\frac{r_0^2 + r^2}{4\kappa_2 t} \right), \quad (\text{A1})$$

where  $I_0(\cdot)$  is a zeroth-order modified Bessel function (LaCasce 2010). In the long-time ( $t \gg \kappa_2^{-1} r$ ,  $r \gg r_0$ ) asymptotic limit,

$$p(r, t) \sim \frac{1}{4\pi\kappa_2 t} \exp \left( -\frac{r^2}{4\kappa_2 t} \right), \quad (\text{A2})$$

which is proportional to the Rayleigh PDF. The second (raw) moment (or relative dispersion) of (A2),

$$\langle r^2 \rangle \sim 4\kappa_2 t, \quad (\text{A3})$$

as expected for a normal diffusive process. The fourth moment normalized by the relative dispersion (or kurtosis) of (A2),

$$\frac{\langle r^4 \rangle}{\langle r^2 \rangle^2} \sim 2, \quad (\text{A4})$$

reflecting the self-similarity of the Rayleigh PDF.

Pair motion is correlated in the turbulent inertial ranges. The Richardson regime corresponds to the energy inertial range (both in 3D and 2D), and the correlated motion sustains local dispersion. With  $E \propto k^{-5/3}$ , the diffusivity has the form  $\kappa_2 = \beta r^{4/3}$  (Richardson 1926; Obhukov 1941; Batchelor 1950), with the constant  $\beta$  is proportional to the third root of the energy dissipation rate. The second-order structure function, which is the inverse Fourier transform of the kinetic energy spectrum, is  $S_2 \propto r^{2/3}$  (Kolmogorov 1941).

The solution to (1) is:

$$p(r, t) = \frac{3}{4\pi\beta t r_0^{2/3} r^{2/3}} I_2 \left( \frac{9r_0^{1/3} r^{1/3}}{2\beta t} \right) \times \exp \left( -\frac{9(r_0^{2/3} + r^{2/3})}{4\beta t} \right), \quad (\text{A5})$$

where  $I_2(\cdot)$  is a second-order modified Bessel function (LaCasce 2010). In the long-time ( $t \gg \beta^{-1} r^{2/3}$ ,  $r \gg r_0$ ) asymptotic limit

$$p(r, t) \sim \left( \frac{3}{2} \right)^5 \frac{1}{\pi(\beta t)^3} \exp \left( -\frac{9r^{2/3}}{4\beta t} \right), \quad (\text{A6})$$

which is the 2D analogue of Richardson's [1926] solution. The relative dispersion associated with (A5) is:

$$\langle r^2 \rangle = \frac{5!}{2} \left( \frac{4\beta t}{9} \right)^3 M \left( 6, 3, \frac{9r_0^{2/3}}{4\beta t} \right) \exp \left( -\frac{9r_0^{2/3}}{4\beta t} \right), \quad (\text{A7})$$

where  $M(\cdot, \cdot, \cdot)$  is the Kummer's function (Graff et al. 2015); its long-time asymptotic limit is given by

$$\langle r^2 \rangle \sim 5.2675\beta^3 t^3. \quad (\text{A8})$$

The kurtosis of (A5) is

$$1 \leq \frac{\langle r^4 \rangle}{\langle r^2 \rangle^2} < 5.6, \quad (\text{A9})$$

(with the equality holding initially), while that of its long-time asymptotic limit (A6) is

$$\frac{\langle r^4 \rangle}{\langle r^2 \rangle^2} \sim 5.6, \quad (\text{A10})$$

which reflects the self-similarity of the Richardson PDF.

Finally, in the enstrophy cascade inertial range, with  $E \propto k^{-3}$ , the diffusivity is  $\kappa_2 = T^{-1} r^2$ , where  $T$  is proportional to the inverse cubic root of the enstrophy dissipation rate (Lin 1972). The corresponding second-order structure function is  $S_2 \propto r^2$  (e.g., Bennett 1984).

The solution to (1) is given by:

$$p(r, t) = \frac{1}{4\pi^{3/2}(t/T)^{1/2} r_0^2} \exp \left( -\frac{(\ln r/r_0 + 2t/T)^2}{4t/T} \right) \quad (\text{A11})$$

(Lundgren 1981; Bennett 2006; LaCasce 2010). The relative dispersion is

$$\langle r^2 \rangle = r_0^2 \exp \frac{8t}{T}, \quad (\text{A12})$$

while the kurtosis is

$$\frac{\langle r^4 \rangle}{\langle r^2 \rangle^2} = \exp \frac{8t}{T}. \quad (\text{A13})$$

The Lundgren PDF (A11) is lognormal and thus not self-similar: it gets more peaked in time, possessing increasingly long tails (at large scales). Note that the same PDF and exponential growth occurs with a kinetic energy spectral slope with  $\alpha > 3$  (Bennett 1984; Babiano et al. 1990).

## APPENDIX B

**The NCOM simulation**

Configured for the GoM, the NCOM simulation employs assimilation and nowcast analyses from NCODA (Navy Coupled Ocean Data Assimilation) (Cummings 2005). Forecasts are generated by systems linking NCODA with regional implementations (Rowley and Mask 2014) of NCOM (Barron et al. 2006). The model has 1-km horizontal resolution and was initiated on 15 May 2012 from the then operational global ocean model Global Ocean Forecast System (GOFS) 2.6 (Barron et al. 2007). Daily boundary conditions are received from the current operational GOFS using the HYbrid Coordinate Ocean Model (HYCOM) (Metzger et al. 2009). The vertical grid is comprised of 49 total levels; 34 terrain-following  $\sigma$ -levels above 550 m and 15 lower  $z$ -levels. The  $\sigma$ -coordinate structure has higher resolution near the surface with the surface layer having 0.5-m thickness. The simulation uses atmospheric forcing at the sea surface from COAMPS (Coupled Ocean/Atmosphere Mesoscale Prediction System) (NRL 1997) to generate forecasts of ocean state out to 72 h in 3-h increments. The observational data assimilated in these studies is provided by NAVOCEANO (Naval Oceanographic Office) and introduced into NCODA via its ocean data quality control process. Observations are three-dimensional variational (3D-Var) assimilated (Smith et al. 2011) in a 24-h update cycle with the first guess from the prior day NCOM forecast.

## APPENDIX C

**The GLAD experiment**

As part of the GLAD experiment, the Consortium for Advanced Research on Transport of Hydrocarbon in the Environment (CARTHE) funded by the BP/Gulf of Mexico Research Initiative deployed more than 300 drifters near the *Deepwater Horizon* site over the period the period 20–31 July 2012.

Most GLAD drifters followed the CODE (Coastal Ocean Dynamics Experiment) design (Davis 1985), with a drogue at 1-m depth that reduces windage and wave motion effects. With an accuracy of 5 m, the drifter were tracked using the GPS (Global Positioning System) system, which transmitted positions every 5 to 15 min. Quarter-hourly drifter trajectory records were obtained from the raw drifter trajectories treated to remove outliers and fill occasional gaps, and also lowpass filtered with a 15-min cut-off.

Except for the initial deployment, which consisted of 20 drifters launched individually on 20 July 2012

over the DeSoto Canyon area, the deployments were carried out in triplets, with the drifters in each triplet separated roughly 100 m from each other. The main deployments consisted of 2 clusters of 30 triplets arranged in S-shaped configurations. One cluster was released on 20 July 2012 centered at (88.1°, 28.8°N) and the other cluster on 20 July 2012 at (87.6°, 29.2°N). Each S-track spanned an area of approximately 8-km  $\times$  10-km and consisted of 10 nodes spaced 2- to 4-km apart. Each node was made up of 3 equilateral triangles with 500-m side. Another cluster of 10 triplets arranged in a triangular configuration spanning an area similar to that spanned by S-shaped configurations was launched on 29 July 2012 near (87.5°, 29.0°N). Two additional clusters with 20 triplets in total were released over 30–31 July 2012 near (89.2°, 27.8°N) inside a cyclonic eddy feature of about 50 km in diameter.

**References**

- Artale, V., G. Boffetta, A. Celani, M. Cencini, and A. Vulpiani, 1997: Dispersion of passive tracers in closed basins: Beyond the diffusion coefficient. *Phys. Fluids*, **9** (3162), 3162–3171.
- Aurell, E., G. Boffetta, A. Crisanti, G. Paladin, and A. Vulpiani, 1997: Predictability in the large: An extension of the concept of Lyapunov exponent. *J. Phys. A: Math. Gen.*, **30**, 1–26.
- Babiano, A., C. Basdevant, P. LeRoy, and R. Sadourny, 1990: Relative dispersion in two-dimensional turbulence. *J. Fluid Mech.*, **214**, 535–557.
- Barron, C. N., A. B. Kara, P. J. Martin, R. C. Rhodes, and L. F. Smedstad, 2006: Formulation, implementation and examination of vertical coordinate choices in the global Navy Coastal Ocean Model (NCOM). *Ocean Modell.*, **11**, 347–375.
- Barron, C. N., L. F. Smedstad, J. M. Dastugue, and O. M. Smedstad, 2007: Evaluation of ocean models using observed and simulated drifter trajectories: Impact of sea surface height on synthetic profiles for data assimilation. *J. Geophys. Res.*, **112**, C07019, doi:0.1029/2006JC002982.
- Batchelor, G. K., 1950: The application of the similarity theory of turbulence to atmospheric diffusion. *Quart. J. Roy. Meteor. Soc.*, **76**, 133–146.
- Bennett, A. F., 1984: Relative dispersion: Local and nonlocal dynamics. *J. Atmos. Sci.*, **41**, 1881–1886.
- Bennett, A. F., 2006: *Lagrangian fluid dynamics*. Cambridge University, Cambridge.
- Callies, J., and R. Ferrari, 2013: Interpreting energy and tracer spectra of upper-ocean turbulence in the submesoscale range (1–200 km). *J. Phys. Oceanogr.*, **43**, 2456–2474.
- Callies, J., R. Ferrari, and O. Bühler, 2014: Transition from geostrophic turbulence to inertia-gravity waves in the atmospheric energy spectrum. *Proc. Nat. Acad. Sci. USA*, **111**, 17033–17038.

- Chant, R. J., 2001: Evolution of near-inertial waves during an upwelling event on the New Jersey inner shelf. *J. Phys. Oceanogr.*, **31**, 746–764.
- Charney, J. G., 1971: Geostrophic turbulence. *J. Atmos. Sci.*, **28**, 1087–1093.
- Chelton, D. B., R. A. deSzoeke, M. G. Schlax, K. El Naggar, and N. Siwertz, 1998: Geographical variability of the first baroclinic rossby radius of deformation. *J. Phys. Oceanogr.*, **28**, 433–460.
- Coelho, E. F., and Coauthors, 2015: Ocean current estimation using a Multi-Model Ensemble Kalman Filter during the Grand Lagrangian Deployment experiment (GLAD). *Ocean Modell.*, **87**, 86–106, doi:10.1016/j.oceomod.2014.11.001.
- Cummings, J. A., 2005: Operational multivariate ocean data assimilation. *Q. J. Royal Meteorol. Soc.*, **131**, 3583–3604.
- Davis, R., 1985: Drifter observations of coastal surface currents during CODE: The method and descriptive view. *J. Geophys. Res.*, **90**, 4741–4755.
- Gill, A. E., 1982: *Atmosphere-Ocean Dynamics*. Academic.
- Graff, L. S., S. Guttu, and J. H. LaCasce, 2015: Relative dispersion in the atmosphere from reanalysis winds. *J. Atmos. Sci.*, **72**, 2769–2785, doi:10.1175/JAS-D-14-0225.1.
- Jacobs, G. A., and Coauthors, 2014: Data assimilation considerations for improved ocean predictability during the Gulf of Mexico Grand Lagrangian Deployment (GLAD). *Ocean Modell.*, **83**, 98–117, doi:10.1016/j.oceomod.2014.09.003.
- Jullien, M.-C., 2003: Dispersion of passive tracers in the direct enstrophy cascade: Experimental observations. *Phys. Fluids*, **5**, 2228.
- Jullien, M.-C., J. Paret, and P. Tabeling, 1999: Richardson pair dispersion in two-dimensional turbulence. *Phys. Rev. Lett.*, **82**, 2872–2875.
- Klein, P., 2009: The oceanic vertical pump induced by mesoscale and submesoscale turbulence. *Ann. Rev. Marine Sci.*, **1**, 351–375.
- Kolmogorov, A. N., 1941: The local structure of turbulence in incompressible viscous fluid for very large reynolds numbers. *Dokl. Akad. Nauk SSSR*, **30**, 9–13.
- Koszalka, I., J. H. LaCasce, and K. A. Orvik, 2009: Relative dispersion in the Nordic Seas. *J. Mar. Res.*, **67**, 411–433.
- Kraichnan, R. H., 1966: Dispersion of particle pairs in homogeneous turbulence. *Phys. Fluids*, **9**, 1937–1943.
- Kraichnan, R. H., 1967: Inertial ranges in two-dimensional turbulence. *Phys. Fluids*, **10**, 1417–1423.
- Kunze, E., 1985: Near inertial wave propagation in geostrophic shear. *J. Phys. Oceanogr.*, **15**, 544–565.
- LaCasce, J. H., 2008: Statistics from Lagrangian observations. *Progr. Oceanogr.*, **77**, 1–29.
- LaCasce, J. H., 2010: Relative displacement probability distribution functions from balloons and drifters. *J. Mar. Res.*, **68**, 433–457.
- LaCasce, J. H., and C. Ohlmann, 2003: Relative dispersion at the surface of the Gulf of Mexico. *J. Mar. Res.*, **61**, 285–312.
- Lin, J.-T., 1972: Relative dispersion in the enstrophy-cascading inertial range of homogeneous two-dimensional turbulence. *J. Atmos. Sci.*, **29**, 394–395.
- Lundgren, T. S., 1981: Turbulent pair dispersion and scalar diffusion. *J. Fluid Mech.*, **111**, 27–57.
- McWilliams, J. C., 2008: Fluid dynamics at the margin of rotational control. *Environ. Fluid Mech.*, **8**, 441–449.
- Metzger, E. J., O. M. Smedstad, and S. N. Carroll, 2009: User’s Manual for Global Ocean Forecast System (GOFS) Version 3.0 (V3.0). NRL Memorandum Report, NRL/MR/7320-09-9175.
- Morel, P., and M. Larcheveque, 1974: Relative dispersion of constant-level balloons in the 200 mb general circulation. *J. Atmos. Sci.*, **31**, 2189–2196.
- Nastrom, G. D., and K. S. Gage, 1985: A climatology of atmospheric wavenumber spectra of wind and temperature observed by commercial aircraft. *J. Atmos. Sci.*, **42**, 950–960.
- NRL, 1997: The Naval Research Laboratory’s Coupled Ocean/Atmosphere Mesoscale Prediction System (COAMPS). Mon. Weather Rev. 125, 1414–1430.
- Obhukov, A. M., 1941: Energy distribution in the spectrum of turbulent flow. *Izv. Akad. Nauk. SSR Ser. Geogr. Geo.*, **5**, 453–466.
- Ohlmann, J. C., and P. P. Niiler, 2005: A two-dimensional response to a tropical storm on the Gulf of Mexico shelf. *Progr. Oceanogr.*, **29**, 87–99.
- Olascoaga, M. J., and Coauthors, 2013: Drifter motion in the Gulf of Mexico constrained by altimetric Lagrangian Coherent Structures. *Geophys. Res. Lett.*, **40**, 6171–6175, doi:10.1002/2013GL058624.
- Poje, A. C., and Coauthors, 2014: The nature of surface dispersion near the Deepwater Horizon oil spill. *Proc. Nat. Acad. Sci. USA*, **111**, 12 693–12 698.
- Pollard, R. T., 1980: Properties of near-surface inertial oscillations. *J. Phys. Oceanogr.*, **10**, 385–398.
- Press, W. H., S. A. Teukolsky, and W. T. Vetterling, 2007: *Numerical Recipes: The Art of Scientific Computing*. 3rd ed., Cambridge University, Cambridge.
- Richardson, L. F., 1926: Atmospheric diffusion on a distance-neighbour graph. *Proc. R. Soc. Lond. A*, **110**, 709–737.
- Rowley, C., and A. Mask, 2014: Regional and coastal prediction with the relocatable ocean nowcast/forecast system. *Oceanography*, **27**, 3, doi:10.5670/oceanog.2014.67.
- Smith, S. R., and Coauthors, 2011: Validation Test Report for the Navy Coupled Ocean Data Assimilation 3D Variational Analysis (NCODA-VAR) System, Version 3.43. NRL Memorandum Report NRL/MR/7320-11-9363.
- Thomas, L., A. Tandon, and A. Mahadevan, 2008: Submesoscale ocean processes and dynamics. *Eddy Resolving*

*Ocean Modeling*, H. Hecht, and H. Hasumi, Eds., AGU, Washington, D. C., 17–38.

Webster, F., 1968: Observations of inertial-period motions in the deep sea. *Rev. Geophys.*, **6**, 473–490.

Young, W. R., and M. B. Jelloul, 1997: Propagation of near-inertial oscillations through a geostrophic flow. *J. Mar Res.*, **55**, 735–766.